

Self-Stabilizing Laser Sails Based on Optical Metasurfaces

Joel Siegel¹ and Anthony Y. Wang

Department of Physics, University of Wisconsin-Madison, Madison, Wisconsin 53606, United States

Sergey G. Menabde²

School of Electrical Engineering, Korea Advanced Institute of Science and Technology, Daejeon 34141, Korea

Mikhail A. Kats

Department of Electrical and Computer Engineering, University of Wisconsin-Madison, Madison, Wisconsin 53606, United States

Min Seok Jang²

School of Electrical Engineering, Korea Advanced Institute of Science and Technology, Daejeon 34141, Korea

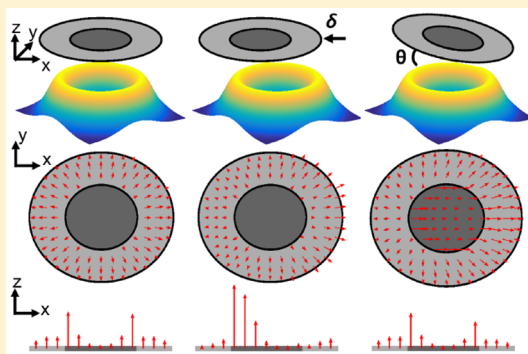
Victor Watson Brar*

Department of Physics, University of Wisconsin-Madison, Madison, Wisconsin 53606, United States

Supporting Information

ABSTRACT: This article investigates the stability of “laser sail”-style spacecraft constructed from dielectric metasurfaces with areal densities $<1 \text{ g/m}^2$. We show that the microscopic optical forces exerted on a metasurface by a high-power laser can be engineered to achieve passive self-stabilization, such that it is optically trapped inside the drive beam and self-corrects against angular and lateral perturbations. The metasurfaces we study consist of a patchwork of beam-steering elements that reflect light at different angles and efficiencies. These properties are varied across the area of the metasurface, and we use optical force modeling tools to explore the behavior of several metasurfaces with different scattering properties as they interact with beams that have different intensity profiles. Finally, we use full-wave numerical simulation tools to extract the actual optical forces that would be imparted on Si/SiO₂ metasurfaces consisting of more than 400 elements, and we compare those results to our analytical models. We find that, under first-order approximations, there are certain metasurface designs that can propel a “laser-sail”-type spacecraft in a stable manner.

KEYWORDS: metasurface, optical force, laser sail, laser propulsion, passive stabilization



The optical properties of a material can be dramatically altered by structuring the material on subwavelength length scales to create a “metamaterial” or, for flat geometries, a “metasurface”. In these systems, the reflection and refraction of light is controlled by engineering the local, microscopic scattering properties. Metasurfaces can be made much thinner than standard optical elements, and recent advances in nanofabrication as well as optical design tools have allowed for the creation of metasurfaces that generate parabolic lenses, constant-angle beam steerers, vortex beams, and holograms,^{1–16} with reflectivities exceeding 99% with low absorptive loss in some cases.^{17–20} While the beam-shaping properties of metasurfaces are well known, the optical forces

present on metasurfaces have been less explored. To understand these forces, consider Figure 1a, which shows a standard metasurface consisting of resonators that scatter light with different phases, reshaping the wavefronts of reflected and transmitted light. Due to momentum conservation, there are both normal and in-plane optical forces generated across the surface that depend on the scattering behavior. These forces are ordinarily small and inconsequential, however, as the laser

Received: March 28, 2019

Published: June 28, 2019

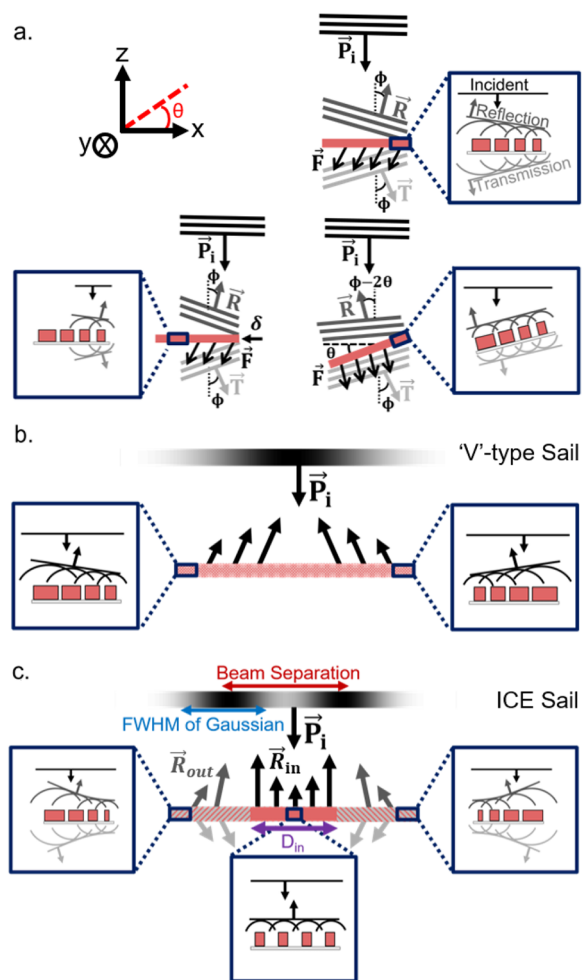


Figure 1. (a) Schematic of dielectric metasurface beam-steerer that deflects an incoming beam at a constant angle, ϕ . In black, the resultant forces created by radiation pressure on a beam-steering metasurface that is centered in the beam (upper right), offset by δ (lower left), tilted by an angle θ (lower right). The coordinate system used in this analysis with a rotation in the x - z plane shown in red (upper left). (b) Cartoon schematic of a “V”-type sail with a Gaussian input beam. (c) Cartoon schematic of an ICE metasurface/sail with a double Gaussian input beam.

power is increased, they can become large enough to impart motion on the metasurface.

One scenario where the optical forces can become large is in “laser sail” powered spacecraft, where, e.g., a 100 GW beam is reflected off a mirror-like “sail”, accelerating it to fraction of the speed of light.²¹ Among the many challenges facing such efforts is the construction of the sail itself, which must display high reflectivity, minimal absorption, low weight, and be large enough such that the beam can focus on it within solar space. A more strenuous requirement is that the sail and payload exhibit self-stability within the laser beam, such that the sail is passively steered to stay in a position of maximum thrust, and desired directionality. In this Article, we show that dielectric metasurfaces provide a promising pathway for realizing a laser sail. By locally controlling the angle and magnitude of reflection/transmission across the sail, metasurfaces can be constructed that enable both efficient propulsion and a passive means of orientation correction that leads to self-stabilizing behavior when driven by a high-power laser.

This paper is split into two parts. We first conduct an analytical study that considers sails constructed of idealized beam-steering components and, by using dynamical modeling tools, we find deflection profiles that optimize for stability, propulsion efficiency, and operational tolerance. Second, we use finite-difference time-domain (FDTD) simulations to model the light-scattering behavior of actual dielectric metasurfaces that are designed to match the optimized force parameters, and we compare how close realistic metasurfaces can match idealized structures.

We note that there are several requirements of a laser sail that we do not directly address in this work. These include potential bending and folding of the sail, the ability of the sail to tolerate relativistic Doppler shifting, the possibility of sail overheating. Those issues are discussed qualitatively at the end of this manuscript, but a comprehensive resolution is left for future studies.

MOTION OF IDEALIZED METASURFACES

Dynamical Force Coefficients. In the simple metasurface beam-steering geometry shown in Figure 1a, the scattered fields from individual optical resonators pick up a linear phase gradient that results in reflected and transmitted wavefronts that are tilted at an angle ϕ with respect to the surface.^{22–24} If the structure is rotated by an angle θ , the optical path length of reflected light changes linearly across the surface, resulting in an additional -2θ in the angle of the reflected light. The transmitted (refracted) light, meanwhile, maintains the same angle of transmittance as the metasurface is rotated. As the light is reflected/refracted, nonzero tangential (F_x) and normal (F_z) forces are imparted on the structure due to momentum conservation of the combined incoming/outgoing photon and metasurface system. For a generalized metasurface interacting with a nonuniform beam (i.e., Gaussian, flat top, donut, etc.), the local beam power, P_i , as well as the reflected light, \vec{R} , and transmitted light, \vec{T} , will all be functions of the position across the metasurface, and the optical forces will have a nontrivial dependence on the metasurface’s rotational or lateral offset relative to the incoming beam. By integrating the optical force and torque contributions across the rigid sail and drive beam, the first-order equations of motion can be written as

$$F = m \frac{\partial^2 \delta}{\partial t^2} = C_1 \delta + C_2 \theta \quad (1)$$

$$\tau = I \frac{\partial^2 \theta}{\partial t^2} = C_3 \delta + C_4 \theta \quad (2)$$

where F and τ are the lateral force and torque acting on the rigid sail, respectively, and δ and θ are the lateral and angular offsets, respectively. $C_{1,2,3,4}$ are the first-order dynamical force coefficients ($\frac{\partial F}{\partial \delta}$, $\frac{\partial F}{\partial \theta}$, $\frac{\partial \tau}{\partial \delta}$, $\frac{\partial \tau}{\partial \theta}$), which are specific for each combination of incident beam and metasurface profile. In this work, we considered metasurfaces that are 4 m wide, with a mass, m , and moment of inertia, I , of 8.5 g and 17 gm², respectively. These parameters were extracted from metasurfaces that are described in more detail in the Full-Wave Simulations section. The coefficients $C_{1,2,3,4}$ were derived by calculating the total forces and torques on the metasurfaces as they are shifted over 2 cm and tilted by up to 0.1°. We find that the linear approximation can be valid for offsets on the order of tens of centimeters and rotations on the order of degrees.

The dynamical force analysis conducted in our work was restricted to a 2D model of the system where the sail has translational invariance along the y axis. The motion of the sail is constrained to translations along the x and z axes and rotations in the x - z plane. This approximation is made so that the sails can be faithfully modeled within our computational restraints in the [Full-Wave Simulations](#) section. We note that this 2D model does not differ significantly from a full 3D model for three reasons. First, assuming a cylindrically symmetric system in 3D, the dynamic force coefficients for the motion along y and rotation about the x axis are identical to the motion along x and rotation about the y axis. Second, we do not assume the sail is spinning about the z axis, so the two types of motion are uncoupled up to a first-order approximation.²⁵ Third, while the dynamic force coefficients change when converting from a 2D model to a 3D model of the system, the general trends and approximate magnitudes of the coefficients remain the same (see [Supporting Information](#)), allowing for conclusions drawn in the 2D case to remain applicable to the 3D situation.

Motion Simulation. Using eqs 1 and 2, we use a “Leapfrog” integration method²⁶ (where the positions and velocities are updated at interleaved time points, such that they “leapfrog” over each other) to simulate the motion of a metasurface in a particular beam profile. We calculate the motion of the metasurface/beam combination in the presence of beam intensity fluctuations or with initial lateral and angular offsets of 1 cm or 0.05° . We find that the sail motion can display a large range of behavior depending on the metasurface structure, as well as the drive-beam profile, and these behaviors can be described as either “stable” or “unstable”. We classify a sail beam combination as “stable” if, during a 60 s period, the sail does not move or rotate beyond 2 cm or 0.1° , respectively. Qualitatively, “stable” sail behavior is manifested as small oscillations about the origin, while “unstable” behavior is characterized as the sail quickly diverging in position and/or angle, as seen in [Figure 2](#).

To illustrate how metasurface structure can enable stability of a laser sail, consider the sail geometry shown in [Figure 1b](#). This design, referred to as a “V”-type sail, reflects light at two constant angles that are equal and opposite on the left and right sides of the sail. When the sail moves to the left (right) relative to an incident Gaussian beam, higher power strikes the right (left) side of the sail, and a force is imparted that pushes the sail back to the right (left), thus, establishing a lateral restoring force. This sail geometry, however, is not stable against rotational offsets, which force the sail to be pushed out of the beam. An advantage of a metasurface sail, however, is that it can exhibit complex reflection and transmission behaviors without distorting the geometrical shape of the surface or changing the constituent materials; as a result, stabilizing force profiles can be generated using realistic structures. As an example, in [Figure 1c](#), we show an “inverted cat eye” (ICE) sail that consists of a highly reflective (reflectance $R_{in} = 95\%$) inner region that reflects the beam normal to the surface, and a more transmissive outer region (reflectance R_{out}) that acts as a “metalens” with a parabolic reflection/transmission profile. When placed in a “donut” beam, modeled as two offset Gaussians in 2D, the ICE geometry can correct for both lateral and rotational offsets, as we show below.

[Figure 2](#) illustrates the motion of four different combinations of sail and incident beam for the same initial offset of 1 cm.

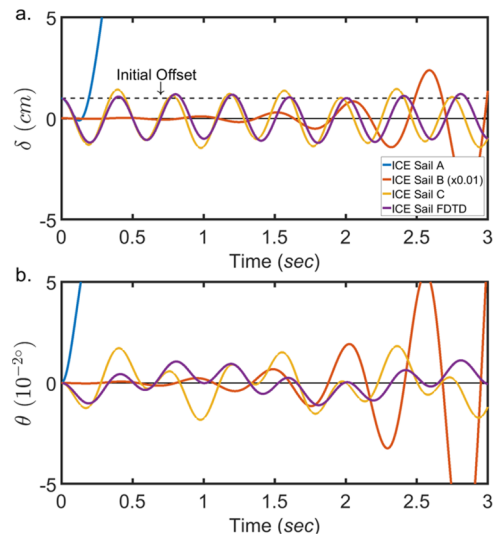


Figure 2. Plots of the displacement (a) and rotation (b) for three different sail and beam combinations over a three second time interval. Each sail is four meters wide with an initial offset of 1 cm. The incident beam power is 100 GW. For the three ICE sails, $R_{out} = 0.3$, $D_{in} = 2$ m, and the incident beam is a double Gaussian with a 1.65 m fwhm. ICE Sail A is for an incident beam with Beam Separation = 1.8 m, ICE Sail B is for an incident beam with Beam Separation = 2.56 m, and ICE Sail C is for an incident beam with Beam Separation = 2.40 m. ICE Sail FDTD is the motion of an FDTD simulated sail (see the [Full-Wave Simulations](#) section for details).

These behaviors can be understood by considering the dynamic force coefficients. ICE sail “A”, shown in [Figure 2](#), has $C_1 < 0$, suggesting stability against lateral offsets, but it also has $C_{2,3} > 0$ and $C_4 \sim 0$, indicating that (1) positive angular rotations create positive lateral forces ($C_2 > 0$); (2) positive lateral offsets create positive torque ($C_3 > 0$); and (3) positive rotations create minimal torque ($C_4 \sim 0$). These conditions create a positive feedback effect between rotation and offset, which quickly destabilizes the sail. This can be described quantitatively by considering that $C_1 C_4 + C_2 C_3 < 0$ is a necessary condition for marginal stability,²⁵ and for $C_4 \ll 1$, this condition cannot be satisfied when $C_{2,3} > 0$.

In contrast, by changing the beam separation of the double Gaussian beam, a negative C_3 value can be realized, meaning positive offsets create negative torques. This provides a route toward a stable sail motion where positive rotational offsets drive positive lateral motion ($C_2 > 0$) which, in turn, creates a negative torque ($C_3 < 0$) that corrects for the initial rotation, leading to small oscillations about the origin ([Figure 2](#), ICE Sail “C”, yellow line). We note, however, that while the $C_1 C_4 + C_2 C_3 < 0$ condition is generally satisfied when $C_3 < 0$, this is not a sufficient condition to predict stable sail behavior, which depends on the relative ratios of $C_{1,2,3,4}$ within a narrow range of parameter space. ICE sail “B”, for example, has a negative C_3 , but displays an oscillatory motion with increasing magnitude and does not achieve stability.

Metasurface Stability Optimization. In order to search for and classify stable ICE sail configurations, we simulated the motion of 4 m wide sails with varying reflection coefficients for the outer region ($R_{out} = 15\%, 30\%$), inner region widths ($D_{in} = 1.33$ m, 2 m), and outer edge deflection angle ($\theta_{max} = 5.7^\circ, 11.4^\circ, \text{ and } 22.6^\circ$) an expanded analysis is shown in the [Supporting Information](#)). We model the motion of these sails in a continuum of double-Gaussian beam profiles with an

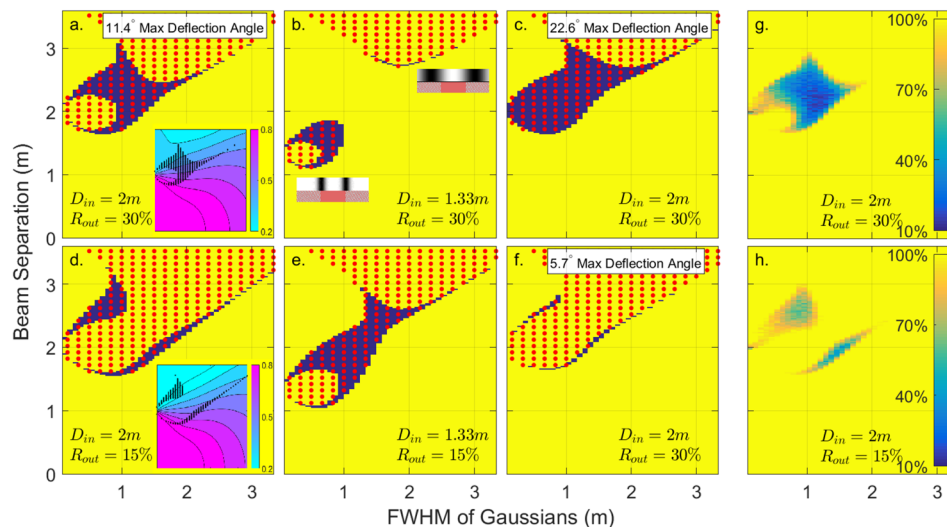


Figure 3. (a–f) Analysis of stability for six ICE-sail configurations driven by double-Gaussian beams with varying beam separation and fwhm for an initial offset of 1 cm. Yellow (purple) regions indicate sails configurations that are unstable (stable). The dotted red areas indicate sail configurations that satisfy the $C_1C_4 + C_2C_3 < 0$ condition. (a, b) ICE sails with $R_{out} = 30\%$ and $D_{in} = 2\text{ m}$, 1.33 m , respectively. Insets in (a, d) show the fraction of maximum thrust achievable for each sail/beam combination and the dotted black areas indicate sails that were stable when initially offset by 1 cm. Insets in (b) show a cartoon of the beams on the sail at those coordinates. (d, e) ICE sails with $R_{out} = 15\%$ and $D_{in} = 2\text{ m}$, 1.33 m , respectively. (c, f) ICE sails with $D_{in} = 2\text{ m}$ and $R_{out} = 30\%$ (similar to a), but their angle of deflection at each point is halved or doubled in comparison to (a), respectively. The motion was simulated over a 60 s period. (g, h) Analysis of stability for two ICE-sail configurations both with $D_{in} = 2\text{ m}$ and $R_{out} = 30\%$ (g) or $R_{out} = 15\%$ (h) reflection efficiencies for their outer regions. The motion of the sail is tracked over 5 min, with 0.12% noise introduced to the beam. Yellow regions indicate sails that failed 100% of the time. Blue indicates regions that maintained the lowest rates of failure.

incident beam composed of two Gaussian beams symmetrically offset from the center, with the beam defined by the fwhm of the Gaussians, and the separation between them. The results of these simulations are shown in Figure 3.

These results demonstrate that stability is strongly dependent on the metasurface profile, as well as the beam shape. Overall, as R_{out} decreases and D_{in} increases, the number of regions that satisfy $C_1C_4 + C_2C_3 < 0$ increases, a result that occurs because these sails can achieve negative values of C_3 for more beam combinations. The number of configurations that show stable sail behavior, however, does not have a strong, intuitive dependence on R_{out} or D_{in} . There is, however, a stronger dependence on the outer edge deflection angle. Figure 3a,c,f compares the stability behaviors of sails that have identical R_{out} and D_{in} values, but with different outer edge deflection angles. These figures indicate that steeper deflection angles (or, equivalently, parabolic lens profiles with shorter focusing distances) allow for more stability conditions and loosen constraints on the drive laser.

In order to determine which sail/beam configurations are “maximally stable”, it is necessary to consider beam intensity profiles that contain time-dependent distortions which, in real world scenarios, could be caused by laser interference (“speckle”) and atmospheric fluctuations, which can destabilize the sail. Here we analyze the sensitivity of metasurface sails to such perturbations by using a Monte Carlo method to introduce randomized, time-varying intensity fluctuations in the beam profile while simulating the motion of the sail. We assume intensity variations that occur over 10 cm characteristic length scales, with time correlations of 1 ms, corresponding to time scales associated with atmospheric turbulence.²⁷ With the fluctuation intensity set to 0.12%, we ran 100 simulations for each configuration shown in Figure 3a,d, and we recorded the probability that a sail maintained stability. The results of those

simulations are shown in Figure 3g,h, where we observe a large variation in stability rates between sail configurations. When $R_{out} = 30\%$ (g), there is a large basin of stability that achieves a failure rate of as low as 13%.

These simulations also help deduce which stable configuration provide maximum thrust, which is plotted in the insets of Figure 3a,d. Considering only beams that have a fwhm $>1.6\text{ m}$ (i.e., realistic, diffraction-limited beams), the maximum thrust achievable with a stable sail/100 GW beam configuration is 370 and 400 N for $R_{out} = 30\%$ and 15% , respectively. For comparison, the maximum theoretical thrust, which occurs when 100% of the light is reflected normally, is 667 N.

■ FULL-WAVE SIMULATIONS

In the *Motion of Idealized Metasurfaces* section, we modeled the behavior of theoretical beam-steering metasurfaces with idealized optical properties. Actual dielectric metasurfaces, however, rely on using dielectric nanostructure arrays designed to control the optical wavefronts of the scattered laser fields, and these structures diverge from ideal behavior due to phase slips in the structure, phase-dependent reflectivity/transmissivity, and interactions between nanoresonators. These effects can potentially create large modifications in the dynamical force coefficients of a metasurface laser sail. In this section, we design and model large-scale ICE metasurfaces and extract the optical forces on those structures as they are tilted and offset in a drive beam. We then compare the dynamical force coefficients of an actual dielectric surface to those of an idealized structure, and show that the self-stability behavior described in the *Motion of Idealized Metasurfaces* section is achievable.

Optical Design. In order to achieve full control of optical wavefronts, it is necessary to engineer a set of dielectric resonators that can scatter light with phase shifts ranging from

0 to 2π , and with arbitrarily small or large reflection/transmission efficiencies. Here we use Si nanoresonators on SiO₂, which have previously been shown to be effective in the construction of metasurfaces with high reflectivity^{17,18} as well as metasurfaces that act as efficient focusing optics. In order to minimize atmospheric losses and absorptive heating losses within the sail, we assume a drive beam wavelength of 1.55 μm . The set of resonators we use in this work are shown in Figure 4a; 470 nm high Si blocks with variable length and width are

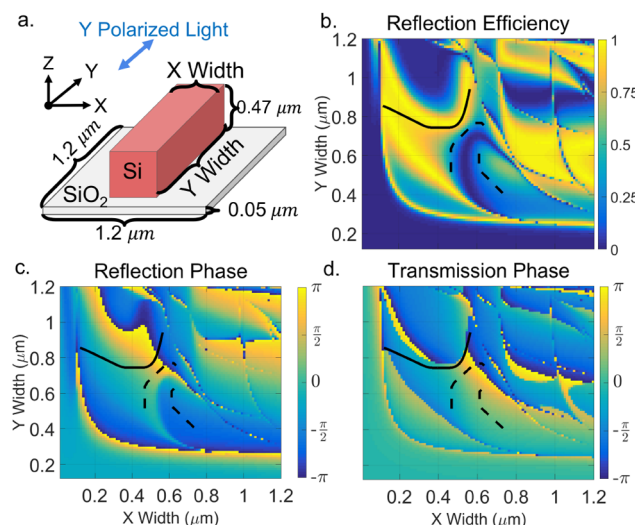


Figure 4. Diagram of the unit cell, reflected magnitude/phase, and transmission phase. (a) Metasurface unit cell consisting of a rectangular block of Si on a SiO₂ membrane. The boundary conditions in the x and y direction are periodic. (b) Magnitude of reflected light as the x and y dimensions of the Si block vary. (c) Phase of reflected light as the x and y dimensions of the Si block vary. (d) Phase of transmitted light as the x and y dimensions of the Si block vary. The solid (dashed) lines indicate a 95% (30%) reflectivity path covering 2π phase.

placed on a 50 nm thick SiO₂ membrane, and the spacing between resonators (center to center) is maintained at a constant 1.2 μm . The scattering properties of these resonators (and all future metasurfaces described in this work) are calculated using a commercial finite-difference time domain tools (Lumerical FDTD). As the resonator dimensions are varied, the magnitude and phase of the reflected/transmitted fields change, as shown in Figure 4b–d. Contours of constant reflectivity that cover the 2π phase can be selected from these plots. Two examples are shown in Figure 4 as solid and dashed lines for 95% and 30% reflectivities, respectively. Note that, for 95% reflectivity, a single continuous path can be chosen, while for 30% reflectivity, two separate paths are required for full phase coverage. Similar contour selection can be performed for reflectivities ranging from 95 to 15%.

The sets of resonators described above can be used to construct metasurfaces as outlined in the first section of this Article and the Motion of Idealized Metasurfaces section, where the magnitude and direction of the reflected/transmitted wavefront is locally controlled by placing resonators with the desired scattering profiles at each location on the surface. This is demonstrated in Figure 5, where we have plotted the electric field profile of the scattered waves from one side of an ICE sail constructed using the nanoresonators in Figure 4. For this metasurface and all others studied below,

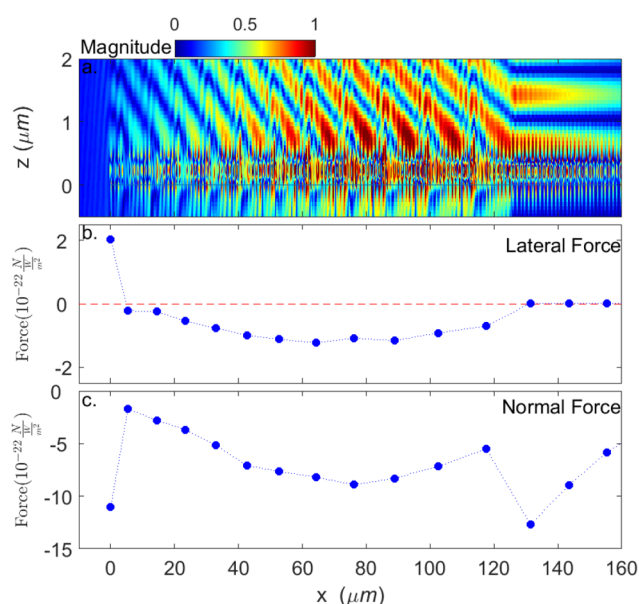


Figure 5. (a) Electric field profile of half of a ICE sail with a reflective (95% reflectivity) inner radius of 127 μm and an outer transmissive (30% reflectivity) region with a parabolic scattering profile where the inner edge steers at 2.8° and the outer edge steers at 5.7°. (b, c) Lateral and normal components of the local forces on the sail, calculated by integrating the Maxwell stress tensor (MST) over a surface that encloses small groups of resonators. For the outer region, the bounding surfaces contain resonator groups that are between phase slips, which range from 5 resonators for the outer edge and 10 resonators inner edge. For the inner, reflective region, the bounding surfaces contain 10 resonators each. The force is normalized using an input beam power of 1 W across the sail.

periodicity is assumed along the y dimension. The structure has a total width of 504 μm , containing 420 individual resonators with constant period of 1.2 μm . The input beam is a “double Gaussian” beam, with a fwhm of 82.9 μm and an annular diameter of 334 μm . The resonators placed from 0 to 125 μm were chosen from the dashed black paths in Figure 4 and provide 30% reflection, along with a parabolic beam-steering profile that ranges from 5.7° at the edge of the sail to 2.8° at the boundary between the outer and inner regions. The inner region is formed by 95% reflective resonators that all have the same phase, which is chosen to match the phase of the innermost resonators of the outer 30% reflective region. Details of how the resonators are chosen at each position are provided in the Supporting Information.

Optical Forces. In order to exhibit the self-stabilized behavior described in the Motion of Idealized Metasurfaces section, it is necessary to design metasurface sails that faithfully generate particular dynamical force coefficients, and that are free from perturbations that could lead to localized folding. Here, we calculate the optical forces locally by integrating the Maxwell Stress Tensor (MST) around boxes enclosing individual resonators or small groups of resonators. We then sum the vector components of those local forces to calculate the overall lateral and normal forces, as well as the torque on the sail as it is tilted and displaced within the beam. In Figure 5b,c, we plot an example of these force components for a metasurface ICE sail illuminated by a double Gaussian beam. These forces display the following expected general trends: (1) there is a lateral force on the outer region that stretches the sail and scales with steering angle and beam intensity; (2) there is

no lateral force on the center region, which is designed to be strictly normally reflecting; and (3) there is a normal force across the sail that scales with beam intensity and sail reflectivity. In this example, we have integrated the MST over a bounding box that groups resonators between phase slips in the metasurface, such that each x, z force shown in Figure 5b,c is determined by calculating the net optical force on groups of 5–10 resonators, depending on the local steering angle. This is done to decrease calculation time, and it has a negligible effect on the calculated net torque or force on the sail, which was confirmed by comparing to calculations where the MST was integrated over individual resonators.

When forces on individual resonators are analyzed, it is observed that there are discontinuities in the force profile that occur due to phase slips and interactions between pairs of resonators, which can cause the actual scattering phase to diverge from the predicted phase. Those effects, which cause anomalies in the scattered E-field profile visible in Figure 5a, are discussed more in the Supporting Information. In most cases, those local discontinuities create forces that are several orders of magnitude weaker than the elastic restoring forces in the underlying SiO₂ slab. However, even when averaged over several resonators, the effects of phase shifts due to resonator interactions can be observable. For example, the depression in lateral forces for the resonators located at $\sim 78 \mu\text{m}$ in Figure 5b is due to such interactions. Moreover, the lateral force reverses sign at the end of the sail due to diffraction from the sail edge, and from the altered scattering properties of the last resonator, which is in an asymmetric environment. For small steering angles, these effects have a minor contribution to the overall forces on the sail; however, as the beam steering angle is increased, so is the frequency of phase slips, which leads to larger adverse contributions to the overall lateral force. Methods for potentially ameliorating and accommodating for such effects are discussed in the Discussion section.

In order to extract the dynamical force coefficient from our simulations, it is necessary to calculate the local optical forces as the metasurface sail is shifted and tilted within the beam and then perform linear fits to the position/tilt versus force/torque dependencies. Figure 6 shows the numerically simulated local forces for offsets of 0 and 40 μm and, separately, rotations of 0° and 3°, for the ICE sail shown in Figure 5. In these plots, we include analytical calculations (lines) of local optical forces for a sail made of ideal beamsteering components, which show good agreement with the forces extracted from the metasurfaces simulated using FDTD. Shifted and rotated simulations were performed over lateral and rotational steps of 5–10 μm and 0.5–1°, respectively, and we found that the force/torque showed a linear dependence on offset/rotation angle over ranges of 20–40 μm and 1–3°. First-order fits were used to determine the effective dynamical force coefficients, $C_{1,2,3,4}$, which are shown in Table 1. We find that the coefficients from an actual dielectric metasurface are of the same sign and order of magnitude as those calculated analytically, but can vary by as much as 40%. These differences can be attributed to the aforementioned phase slips and inter-resonator interactions which add distortions to the reflected/transmitted phase fronts of the scattered light, and can also lead changes in the overall reflection coefficients.

The overall stability of the ICE metasurface sail can be tested by using the dynamical force coefficients in Table 1, along with the methods described in the Motion of Idealized Metasurfaces section. However, to test the viability of a 4 m

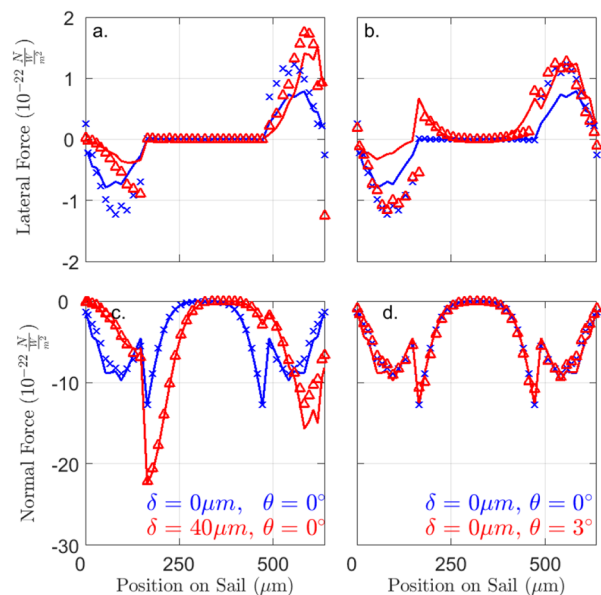


Figure 6. Local lateral (x) and normal (z) components of the optical forces along the sail shown in Figure 5, calculated from the full-wave simulations (blue \times s and red triangles) or using the methods described in the Motion of Idealized Metasurfaces section (solid blue/red lines). (a) Force in the x direction when the sail is offset. (b) Force in the x direction when the sail is rotated. (c) Force in the z direction when the sail is offset. (d) Force in the z direction when the sail is rotated. In all plots, the unoffset, unshifted force is shown in blue and the offset or rotated force is shown in red.

metasurface, these coefficients must be scaled accordingly as the beam size (annulus and fwhm of individual Gaussians) and sail size are increased by $\sim 8000\times$. Such scaling has no effect on C_2 or C_3 , but C_1 will scale inversely with size, while C_4 will scale linearly with size. This behavior was confirmed by calculating $C_{1,2,3,4}$ analytically for 504 μm and 4 m ICE sails with equivalent ratios for reflective/transmissive regions and equivalent steering angles. An analysis of these scaling laws is provided in the Supporting Information. The resulting scaled dynamical coefficients for a 4 m ICE metasurface sail are given in the bottom row of Table 1. Using these values, we can model the motion of a sail with an initial lateral offset of 1 cm, which is shown in Figure 7. These results show that a metasurface sail constructed from Si nanoresonators can exhibit self-stability within a drive beam for over 300 s without ever leaving the range where the linear approximation is valid and exhibiting behavior that closely resembles the motion of the idealized structures discussed in the Motion of Idealized Metasurfaces section.

DISCUSSION

The combined results of the Motion of Idealized Metasurfaces and the Full-Wave Simulations sections show that dielectric metasurfaces offer a viable pathway for creating laser sails that maintain directionality and stability within high-power laser beams. In order to comprehend the real world speed that such a metasurface sail may achieve, we can consider a 100 GW drive laser constructed from a 100 km diameter ground-based array of projectors. Operating at a wavelength of 1.55 μm and for distances of up to 10^8 km, such a beam can maintain features with a fwhm of 1.67 m, which, in an assumed annular geometry, would generate a thrust of ~ 360 N and allow for

Table 1. Dynamic Force Coefficients of an ICE Sail^a

ICE sail	$C_1 \left(\frac{N}{Wm}\right)$	$C_2 \left(\frac{N}{Wdeg}\right)$	$C_3 \left(\frac{N}{W}\right)$	$C_4 \left(\frac{Nm}{Wdeg}\right)$
ideal	-1.43×10^{-6}	6.06×10^{-11}	-2.23×10^{-10}	1.03×10^{-15}
full-wave	-1.79×10^{-6}	4.13×10^{-11}	-2.23×10^{-10}	3.00×10^{-15}
full-wave scaled	-2.29×10^{-10}	4.13×10^{-11}	-2.23×10^{-10}	2.36×10^{-11}

^aThe full-wave dynamic force coefficients scaled up to a 4 m wide sail are shown as well.

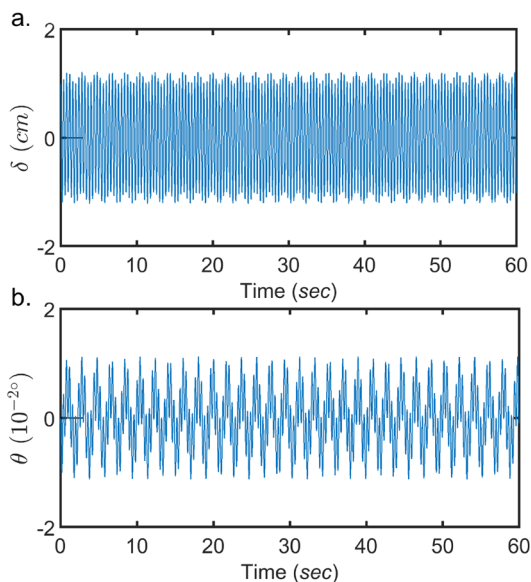


Figure 7. Motion (a) and rotation (b) of an FDTD simulated sail with an initial offset of 1 cm for 60 s.

self-stable behavior for the sail modeled in Figure 7. The weight of such a sail is ~ 8.5 g, and if we assume a 5 g payload, these conditions would allow for final velocities of $0.21c$ to be achieved in ~ 50 min, after which the craft travels too far to project a laser shape that yields stability.²⁸ In addition to self-stability and a high achievable velocity, we note that the ICE sails discussed in this work contain an outer region that can be utilized as a parabolic collimator with a 4 m aperture that could potentially be used to transmit a signal from the craft.

While these results are promising, the analysis presented in this work makes several assumptions and simplifications; ultimately the design of a metasurface laser sail will require new breakthroughs in metasurface architectures, more powerful simulation tools, and the development of new constituent materials. The key issues we would like to address are as follows:

Folding, Strain, and Local Forces. Throughout this work, we have assumed that the metasurface sail maintains a rigid flat shape, regardless of local force gradients. In a real world situation, however, a 50 nm thick SiO_2 substrate will bend and fold over both macroscopic and microscopic length scales. Those perturbations will alter the optical performance of the metasurface, and second-generation designs must incorporate mitigation strategies for such effects. The primary cause of microscopic strain, which occurs between 2 and 10 nanoresonators, is interactions between resonators, which alters their scattering properties such that the beam fronts and optical forces are distorted. Those effects can be compensated for by using inverse design and optimization methods that consider such interactions and adjust resonator shape accordingly.^{12,29} Such methods should not only allow for the

creation of metasurfaces with smoother force profiles, but they could also enable higher scattering angles, which increases the lateral forces. More problematic is the macroscopic strain, which occurs due to nonuniform beam intensity and changes in the metasurface reflectivity. Figure 5c, for example, shows that the normal forces on the sail is not constant, which will lead to bowing of the sail. In order to correct for those effects, it is necessary to design a sail with a favorable relationships between structure and light scattering such that, for example, outwardly bowed surfaces reflect light less. Alternatively, metasurface sails that exhibit stability within flat beam profiles would suffer less from such effects, or metasurface elements that pull outwardly on the sail can be incorporated. We note that the ICE sail design contains some elements of this latter concept, with the edges of the sail scattering at steeper angles and generating larger lateral forces which pull the sail taut. The strain issue can also be addressed by exploring new materials systems. While Si membranes fabricated from SOI display compressive strain, SiN membranes have intrinsic tensile strain, and, when fabricated into photonic crystal geometries, have been recently shown to have reflectivities $>90\%$ for 56 nm membrane thicknesses, making them a promising candidate material system.³⁰ Finally, we note that abnormal optical forces are easily generated on the rim of the sail, where edge diffraction can result in large distortions in the scattered beam fronts. Those effects must be compensated for by designing metasurface edges that minimize diffraction or by using drive beams that have negligible intensity on the edge of the sail.

Doppler Shift. The metasurfaces discussed in the Full-Wave Simulations section are designed to work at a single fixed wavelength ($1.55 \mu\text{m}$), while relativistic light propulsions requires a reflectors that works across a range of Doppler shifted frequencies. Achieving velocities up to $0.21c$, for example, requires a metasurface that exhibits effective propulsion and self-stability from 1.55 to $1.92 \mu\text{m}$. Typically, the scattering phase of an individual nanoresonator is dependent on wavelength and that dependence can lead to distorted beamfronts, and local optical forces that disturb self-stabilizing motion. However, we note that the design of broadband, achromatic metasurfaces that shape light equally across many wavelengths is an active area of research,^{31,41,43} and those methods can be applied to the metasurface laser sail problem.

Absorptive Heating. In this work, we have assumed that the high-power laser imparts optical forces on the metasurface sail without heating it. In fact, some fraction of the light will be absorbed by the sail due to intrinsic properties of the constituent materials and defects, and that absorption will increase the sail temperature. A final, steady state temperature is reached when the power absorbed at the laser wavelengths is equal to the thermal power radiated over all wavelengths. An accurate estimate of this final temperature requires full-angle simulations over all wavelengths, using precise values of the

temperature-dependent extinction coefficients of Si and SiO₂, which is left for future work. However, by using published room temperature values for Si and SiO₂,^{32–36} we can estimate a wavelength-integrated emissivity of 0.05, and an absorptivity at 1.55 μm near 10⁻⁵, yielding a final temperature of ~2200 K—outside the range of the melting points of Si (1687 K) and SiO₂ (1983 K). This temperature can be systematically decreased by engineering the structure to have higher emissivities or lower absorption by changing the constituent materials, or by layering and/or shaping the material stack. For example, it has been shown that the inclusion of mid-IR resonators can enhance the emissivity of metals and polar materials,^{37–39} and that thin, structured material films can display novel thermal-emission properties.^{40,42} Using these methods to increase the emissivity to 0.5, for example, would result in a steady state temperature of ~1200 K.

Residual Motion. The force models used in the [Motion of Idealized Metasurfaces](#) section were first-order and did not include damping terms, which lead to an oscillatory sail motion that did not decay in magnitude. In order to achieve true stability, however, it is necessary to discover conditions where the amplitude of oscillation is reduced to zero, which prevents lateral motion or rotations that would persist after the drive laser is turned off. Optical damping terms could potentially be included through Doppler effects, however, such methods would require relativistic lateral motion, and unrealistic fabrication parameters. More promising is to incorporate some hysteretic motion in the sail whereby, for example, some bending in the sail leads to changes in the optical scattering that is dependent on the velocity. Such stabilization methods are used in other mechanical systems,⁴⁴ and they are an attractive option for laser sail applications, where no obvious damping method exists.

In conclusion, we have studied the use of dielectric metasurfaces to act as laser sails for relativistic, interstellar spacecraft. We have shown that the ability of metasurfaces to reshape optical beamfronts can also be used to control local optical forces, and for extremely high-power lasers, those forces can impart an optical trapping-like effect on the metasurface. That effect is potentially useful for stabilizing laser sails and we find a large parameter space that such behavior is expected to occur. These results represent a new area of metasurface research that will benefit greatly from recent advances in metasurface design, and also introduce new challenges for the nanophotonics community.

■ ASSOCIATED CONTENT

Supporting Information

The Supporting Information is available free of charge on the ACS Publications website at DOI: [10.1021/acsp Photonics.9b00484](https://doi.org/10.1021/acsp Photonics.9b00484).

Description of Local Forces on Sail, Accuracy of “leapfrog” integration technique, “V”-type sail motion, Constants for ICE Sail, Expanded Stability Analysis, Noise Simulations, 3D Model Comparison, Simulation Methods, Optical Force Abnormalities, Extracting Dynamic Force Coefficients, Scaling Laws, and Temperature derived from Stefan–Boltzmann Law (PDF)

■ AUTHOR INFORMATION

Corresponding Author

*E-mail: vbrar@wisc.edu.

ORCID

Joel Siegel: [0000-0002-7344-4839](https://orcid.org/0000-0002-7344-4839)

Sergey G. Menabde: [0000-0001-9188-8719](https://orcid.org/0000-0001-9188-8719)

Min Seok Jang: [0000-0002-5683-1925](https://orcid.org/0000-0002-5683-1925)

Funding

V.W.B. and J.S. were supported by a Defense Advanced Research Projects Agency Young Faculty Award (YFA D18AP00043). S.G.M. and M.S.J. acknowledge support by the National Research Foundation of Korea (NRF) grants funded by the Korea government (MSIT) (2017R1E1A1A01074323 and 2016M3D1A1900038). M.A.K. is supported by the Air Force Office of Scientific Research (FA9550-18-1-0146)

Notes

The authors declare no competing financial interest.

■ ACKNOWLEDGMENTS

This research was performed using the compute resources and assistance of the UW-Madison Center For High Throughput Computing (CHTC) in the Department of Computer Sciences. The CHTC is supported by UW-Madison, the Advanced Computing Initiative, the Wisconsin Alumni Research Foundation, the Wisconsin Institutes for Discovery, and the National Science Foundation, and is an active member of the Open Science Grid, which is supported by the National Science Foundation and the U.S. Department of Energy’s Office of Science. The authors thank Zachary Manchester for useful discussions.

■ REFERENCES

- (1) Aieta, F.; Kats, M. A.; Genevet, P.; Capasso, F. Multiwavelength achromatic metasurfaces by dispersive phase compensation. *Science* **2015**, *347*, 1342–1345.
- (2) Cheng, J.; Ansari-Oghol-Beig, D.; Mosallaei, H. Wave manipulation with designer dielectric metasurfaces. *Opt. Lett.* **2014**, *39*, 6285.
- (3) Decker, M.; Staude, I.; Falkner, M.; Dominguez, J.; Neshev, D. N.; Brener, I.; Pertsch, T.; Kivshar, Y. S. High-efficiency dielectric huygens’ surfaces. *Adv. Opt. Mater.* **2015**, *3*, 813.
- (4) Devlin, R. C.; Khorasaninejad, M.; Chen, W. T.; Oh, J.; Capasso, F. Broadband high-efficiency dielectric metasurfaces for the visible spectrum. *Proc. Natl. Acad. Sci. U. S. A.* **2016**, *113*, 10473.
- (5) Fattal, D.; Li, J.; Peng, Z.; Fiorentino, M.; Beausoleil, R. G. Flat dielectric grating reflectors with focusing abilities. *Nat. Photonics* **2010**, *4*, 466.
- (6) Huang, L.; Chen, X.; Mühlenbernd, H.; Zhang, H.; Chen, S.; Bai, B.; Tan, Q.; Jin, G.; Cheah, K.-W.; Qiu, C.-W. Three-dimensional optical holography using a plasmonic metasurface. *Nat. Commun.* **2013**, *4*, na.
- (7) Karimi, E.; Schulz, S. A.; De Leon, I.; Qassim, H.; Upham, J.; Boyd, R. W. Generating optical orbital angular momentum at visible wavelengths using a plasmonic metasurface. *Light: Sci. Appl.* **2014**, *3*, e167.
- (8) Khorasaninejad, M.; Aieta, F.; Kanhaiya, P.; Kats, M. A.; Genevet, P.; Rousso, D.; Capasso, F. Achromatic metasurface lens at telecommunication wavelengths. *Nano Lett.* **2015**, *15*, 5358–5362.
- (9) Lin, D.; Fan, P.; Hasman, E.; Brongersma, M. L. Dielectric gradient metasurface optical elements. *Science* **2014**, *345*, 298–302.
- (10) Ma, Z.; Hanham, S. M.; Albella, P.; Ng, B.; Lu, H. T.; Gong, Y.; Maier, S. A.; Hong, M. Terahertz all-dielectric magnetic mirror metasurfaces. *ACS Photonics* **2016**, *3*, 1010–1018.
- (11) Ni, X.; Kildishev, A. V.; Shalaev, V. M. Metasurface holograms for visible light. *Nat. Commun.* **2013**, *4*, na.

- (12) Sell, D.; Yang, J.; Doshay, S.; Yang, R.; Fan, J. A. Large-angle, multifunctional metagratings based on freeform multimode geometries. *Nano Lett.* **2017**, *17*, 3752–3757.
- (13) West, P. R.; Stewart, J. L.; Kildishev, A. V.; Shalae, V. M.; Shkunov, V. V.; Strohkendel, F.; Zakharenkov, Y. A.; Dodds, R. K.; Byren, R. All-dielectric subwavelength metasurface focusing lens. *Opt. Express* **2014**, *22*, 26212.
- (14) Yang, Y.; Wang, W.; Moitra, P.; Kravchenko, I. I.; Briggs, D. P.; Valentine, J. Dielectric meta-reflectarray for broadband linear polarization conversion and optical vortex generation. *Nano Lett.* **2014**, *14*, 1394–1399.
- (15) Zhao, W.; Liu, B.; Jiang, H.; Song, J.; Pei, Y.; Jiang, Y. Full-color hologram using spatial multiplexing of dielectric metasurface. *Opt. Lett.* **2016**, *41*, 147–150.
- (16) Zheng, G.; Möhlenbernd, H.; Kenney, M.; Li, G.; Zentgraf, T.; Zhang, S. Metasurface holograms reaching 80% efficiency. *Nat. Nanotechnol.* **2015**, *10*, 308–312.
- (17) Moitra, P.; Slovick, B. A.; Gang Yu, Z.; Krishnamurthy, S.; Valentine, J. Experimental demonstration of a broadband all-dielectric metamaterial perfect reflector. *Appl. Phys. Lett.* **2014**, *104*, 171102.
- (18) Moitra, P.; Slovick, B. A.; Li, W.; Kravchenko, I. I.; Briggs, D. P.; Krishnamurthy, S.; Valentine, J. Large-scale all-dielectric metamaterial perfect reflectors. *ACS Photonics* **2015**, *2*, 692–698.
- (19) Wang, Y.; Kanamori, Y.; Ye, J.; Sameshima, H.; Hane, K. Fabrication and characterization of nanoscale resonant gratings on thin silicon membrane. *Opt. Express* **2009**, *17*, 4938.
- (20) Ye, J.-S.; Matsuyama, N.; Kanamori, Y.; Hane, K. Silicon suspended resonant grating filters fabricated from a silicon-on-insulator wafer. *IEEE Photonics Technol. Lett.* **2008**, *20*, 851.
- (21) Ilic, O.; Went, C. M.; Atwater, H. A. Nanophotonic heterostructures for efficient propulsion and radiative cooling of relativistic light sails. *Nano Lett.* **2018**, *18*, 5583–5589.
- (22) Holloway, C. L.; Kuester, E. F.; Gordon, J. A.; O'Hara, J.; Booth, J.; Smith, D. R. An overview of the theory and applications of metasurfaces: The two-dimensional equivalents of metamaterials. *IEEE Antennas and Propagation Magazine* **2012**, *54*, 10.
- (23) Yu, N.; Capasso, F. Flat optics with designer metasurfaces. *Nat. Mater.* **2014**, *13*, 139–150.
- (24) Yu, N.; Genevet, P.; Kats, M. A.; Aieta, F.; Tetienne, J.-P.; Capasso, F.; Gaburro, Z. Light propagation with phase discontinuities: Generalized laws of reflection and refraction. *Science* **2011**, *334*, 333–337.
- (25) Manchester, Z.; Loeb, A. Stability of a light sail riding on a laser beam. *Astrophys. J., Lett.* **2017**, *837*, L20.
- (26) Birdsall, C. K.; Langdon, A. B. *Plasma Physics via Computer Simulation*; McGraw-Hill, 1985.
- (27) Deserno, M. *How to Generate Exponentially Correlated Gaussian Random Numbers*; UCLA, 2002.
- (28) McInnes, C. R. *Solar Sailing: Technology, Dynamics, and Mission Applications*; Springer, 2004.
- (29) Miller, O. Photonic Design: From Fundamental Solar Cell Physics to Computational Inverse Design. PhD thesis, University of California, Berkeley, 2012.
- (30) Moura, J. P.; Norte, R. A.; Guo, J.; Schäfermeier, C.; Gröblacher, S. Centimeter-scale suspended photonic crystal mirrors. *Opt. Express* **2018**, *26*, 1895.
- (31) Khorasaninejad, M.; Aieta, F.; Kanhaiya, P.; Kats, M. A.; Genevet, P.; Rousso, D.; Capasso, F. Achromatic metasurface lens at telecommunication wavelengths. *Nano Lett.* **2015**, *15*, 5358–5362.
- (32) Kitamura, R.; Pilon, L.; Jonasz, M. Optical constants of silica glass from extreme ultraviolet to far infrared at near room temperature. *Appl. Opt.* **2007**, *46*, 8118.
- (33) Ravindra, N.; Abedrabbo, S.; Chen, W.; Tong, F.; Nanda, A.; Speranza, A. Temperature-dependent emissivity of silicon-related materials and structures. *IEEE Transactions on Semiconductor Manufacturing* **1998**, *11*, 30–39.
- (34) Satō, T. Spectral emissivity of silicon. *Jpn. J. Appl. Phys.* **1967**, *6*, 339–347.
- (35) Schinke, C.; Peest, P. C.; Schmidt, J.; Brendel, R.; Bothe, K.; Vogt, M. R.; Kröger, I.; Winter, S.; Schirmacher, A.; Lim, S.; et al. Uncertainty analysis for the coefficient of band-to-band absorption of crystalline silicon. *AIP Adv.* **2015**, *5*, 067168.
- (36) Timans, P. J. Emissivity of silicon at elevated temperatures. *J. Appl. Phys.* **1993**, *74*, 6353–6364.
- (37) Arnold, C.; Marquier, F.; Garin, M.; Pardo, F.; Collin, S.; Bardou, N.; Pelouard, J.-L.; Greffet, J.-J. Coherent thermal infrared emission by two-dimensional silicon carbide gratings. *Phys. Rev. B: Condens. Matter Mater. Phys.* **2012**, *86*, na.
- (38) Liu, X.; Tyler, T.; Starr, T.; Starr, A. F.; Jokerst, N. M.; Padilla, W. J. Taming the blackbody with infrared metamaterials as selective thermal emitters. *Phys. Rev. Lett.* **2011**, *107*, na.
- (39) Streier, W.; Law, S.; Rosenberg, A.; Roberts, C.; Podolskiy, V. A.; Hoffman, A. J.; Wasserman, D. Engineering absorption and blackbody radiation in the far-infrared with surface phonon polaritons on gallium phosphide. *Appl. Phys. Lett.* **2014**, *104*, 131105.
- (40) Kats, M. A.; Blanchard, R.; Zhang, S.; Genevet, P.; Ko, C.; Ramanathan, S.; Capasso, F. Vanadium dioxide as a natural disordered metamaterial: Perfect thermal emission and large broadband negative differential thermal emittance. *Phys. Rev. X* **2013**, *3*, na.
- (41) Wang, B.; Dong, F.; Li, Q.-T.; Yang, D.; Sun, C.; Chen, J.; Song, Z.; Xu, L.; Chu, W.; Xiao, Y.-F.; et al. Visible-frequency dielectric metasurfaces for multiwavelength achromatic and highly dispersive holograms. *Nano Lett.* **2016**, *16*, 5235–5240.
- (42) Wu, S.-H.; Chen, M.; Barako, M. T.; Jankovic, V.; Hon, P. W.; Sweatlock, L. A.; Povinelli, M. L. Thermal homeostasis using microstructured phase-change materials. *Optica* **2017**, *4*, 1390.
- (43) Wang, S.; Wu, P. C.; Su, V.-C.; Lai, Y.-C.; Chu, C. H.; Chen, J.-W.; Lu, S.-H.; Chen, J.; Xu, B.; Kuan, C.-H. Broadband achromatic optical metasurface devices. *Nat. Commun.* **2017**, *8*, na.
- (44) Semenov, M. E.; Shevlyakova, D. V.; Meleshenko, P. A. Inverted pendulum under hysteretic control: stability zones and periodic solutions. *Nonlinear Dynamics* **2014**, *75*, 247–256.